7. Three–Dimensional Nanostructure Fabrication by Focused Ion Beam Chemical Vapor Deposition

Shinji Matsui

In this chapter, we describe three–dimensional nanostructure fabrication using 30 keV Ga$^+$ focused ion beam chemical vapor deposition (FIB–CVD) and a *phenanthrene* ($C_{14}H_{10}$) source as a precursor. We also consider microstructure plastic art, which is a new field that has been made possible by microbeam technology, and we present examples of such art, including a *micro wine glass* with an external diameter of 2.75 µm and height of 12 µm. The film deposited during such a process is diamond–like amorphous carbon, which has a Young's modulus exceeding 600 GPa, appearing to make it highly desirable for various applications. The production of three–dimensional nanostructure is discussed. The fabrication of microcoils, nanoelectrostatic actuators, and 0.1 µm nanowiring – all potential components of nanomechanical systems – is explained. The chapter ends by describing the realization of nanoinjectors and nanomanipulators, novel nanotools for manipulation and analyzing subcellular organelles.

Electron beams (EBs) and focused ion beam (FIBs) have been used to fabricate various two-dimensional nanostructure devices such as single-electron transistors and metal–oxide–semiconductor (MOS) transistors with nanometer gate lengths. Ten-nanometer structures can be formed by using a commercially available EB or FIB system with 5–10 nm-diameter beams and high-resolution resist [7.1]. Two-dimensional nanostructure fabrication is therefore already an established process. There are various approaches to three-dimensional fabrication using a laser, an EB, or a FIB to perform chemical vapor deposition (CVD). FIB- and EB-CVD are superior to laser-CVD [7.2] in terms of spatial resolution and beam-scan control. *Koops* et al. demonstrated some applications such as an atomic force microscopy (AFM) tip and a field emitter that were realized using EB-CVD [7.3]. *Blauner* et al. demonstrated pillars and walls with high aspect ratios achieved using FIB-CVD [7.4].

The deposition rate of FIB-CVD is much higher than that of EB-CVD due to factors such as the difference in mass between an electron and an ion. Furthermore, the smaller penetration depth of ions compared with electrons makes it easier to create complicated three-dimensional nanostructures. For example, when we attempt to make a coil nanostructure with line width of 100 nm, 10–50 keV electrons pass through the ring of the coil and reach the substrate because of the large range of electrons (at least a few microns), which makes it difficult to create a coil nanostructure using EB-CVD. On the other hand, since the range of ions is a few tens of nanometers or less, the ions are deposited in-

side the ring. Up to now, the realization of complicated nanostructures using FIB-CVD has not been reported.

Therefore, this chapter reports on complicated three-dimensional nanostructure fabrication using FIB-CVD.

7.1 Three-Dimensional Nanostructure Fabrication

We used two commercially available FIB systems (SMI9200, SMI2050, SII Nanotechnology Inc., Tokyo, Japan) with a Ga^+ ion beam operating at 30 keV. The FIB-CVD used a *phenanthrene* ($C_{14}H_{10}$) precursor as the source material. The beam diameter of the SMI9200 system was about 7 nm and that of the SMI2050 system was about 5 nm. The SMI9200 system was equipped with two gas sources in order to increase the gas pressure. The nozzles faced each other and were directed at the beam point. The nozzles were set a distance of 40 μm from each other and positioned about 300 μm above the substrate surface. The inside diameter of a nozzle was 0.3 mm. The *phenanthrene* gas pressure during pillar growth was typically 5×10^{-5} Pa in the specimen chamber, but the local gas pressure at the beam point was expected to be much higher. The crucible of the source was heated to 85 °C. The SMI2050 system, on the other hand, was equipped with a single gas nozzle. The FIB is scanned in order to be able to write the desired pattern via computer control, and the ion dose is adjusted to deposit a film of the desired thickness. The experiments were carried out at room temperature on a silicon substrate.

The deposited film was characterized by observing it with a transmission electron microscope (TEM) and analyzing its Raman spectra. A thin film of carbon (200 nm thick) was deposited on a silicon substrate by 30 keV Ga^+ FIB using *phenanthrene* precursor gas. The

cross sections of the structures created and their electron diffraction patterns were observed by using a 300 kV TEM. There were no crystal structures in the TEM images and diffraction patterns. It was therefore concluded that the deposited film was amorphous carbon (a-C).

Raman spectra of the a-C films were measured at room temperature with the 514.5 nm line of an argon-ion laser. The Raman spectra were recorded using a monochromator equipped with a charge-coupled device (CCD) multichannel detector. Raman spectra were measured at 0.1–1.0 mW to avoid thermal decomposition of the samples. A relatively sharp Raman band at 1550 cm^{-1} and a broad-shouldered band at around 1400 cm^{-1} were observed in the spectra excited by the 514.5 nm line. Two Raman bands were plotted after Gaussian line shape analysis. These Raman bands, located at 1550 and 1400 cm^{-1}, originate from the trigonal (sp^2) bonding structure of graphite and tetrahedral (sp^3) bonding structure of diamond. This result suggests that the a-C film deposited by FIB-CVD is diamond-like amorphous carbon (DLC), which has attracted attention due to its hardness, chemical inertness, and optical transparency.

7.1.1 Fabrication Process

Beam-induced chemical vapor deposition (CVD) is widely used in the electrical device industry for repair of chips and masks. This type of deposition is mainly done on two-dimensional (2-D) pattern features, but it can also be used to fabricate a three-dimensional (3-D) object. *Koops* et al. demonstrated nanoscale 3-D structure construction [7.3] by applying electron-beam-induced amorphous carbon deposition onto a micro vacuum tube. However, focused ion beam (FIB)-induced CVD seems to have many advantages for the fabrication of 3-D nanostructures [7.4–6]. The key issue to realizing such 3-D nanostructures is the short penetration depth of the ions (a few tens of nm) into the target material, being much shorter than that of electrons (several hundreds of μm). This short penetration depth reduces the dispersion area of the secondary electrons, and so the deposition area is restricted to roughly several tens of nanometers. A 3-D structure usually contains overhang structures and hollows. Gradual position scanning
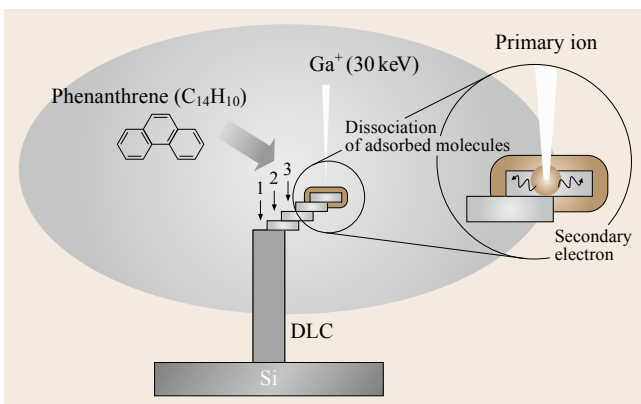

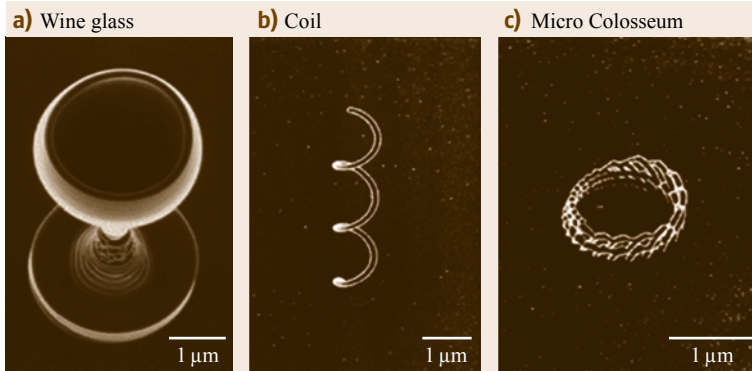**Fig. 7.1** Fabrication process for three-dimensional nanostructure by FIB-CVD

a) Wine glass   **b)** Coil   **c)** Micro Colosseum

1 μm   1 μm   1 μm

Fig. 7.2 (a) Micro wine glass with an external diameter of 2.75 μm and a height of 12 μm. **(b)** Microcoil with coil diameter of 0.6 μm, coil pitch of 0.7 μm, and line width of 0.08 μm. **(c)** *Micro Colosseum*

of the ion beam during the CVD process causes the position of the growth region around the beam point to shift. When the beam point reaches the edge of the wall, secondary electrons appear at the side of the wall and just below the top surface. The DLC then starts to grow laterally; the width of the lateral growth is also about 80 nm. Therefore, by combining the lateral growth mode with rotating beam scanning, it is possible to obtain 3-D structures with rotational symmetry, such as a wine glass.
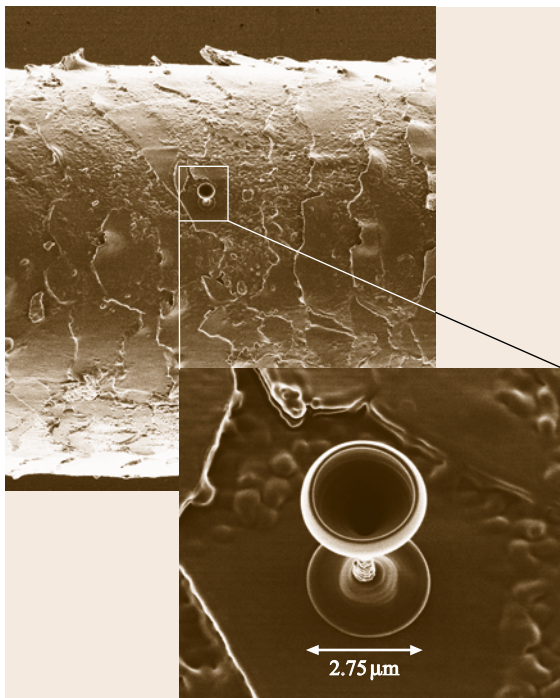
The process of fabricating three-dimensional structures by FIB-CVD is illustrated in Fig. 7.1 [7.7]. In FIB-CVD processes, the beam is scanned in digital mode. First, a pillar is formed on the substrate by fixing the beam position (position 1). After that, the beam position is moved to within a diameter of the pillar (position 2) and then fixed until the deposited terrace thickness exceeds the range of the ions (a few tens of nm). This process is repeated to make three-dimensional structures. The key point to making three-dimensional structures is to adjust the beam scan speed so that the ion beam remains within the deposited terrace, which means that the terrace thickness always exceeds the range of the ions. Growth in the *x*- and *y*-directions is controlled by both beam deflectors. The growth in the *z*-direction is determined by the deposition rate; that is, the height of the structure is proportional to the irradiation time when the deposition rate is constant.

We intend to open up a new field of microstructure plastic art using FIB-CVD. To demonstrate the possibilities of this field, a *micro wine glass* created on a Si
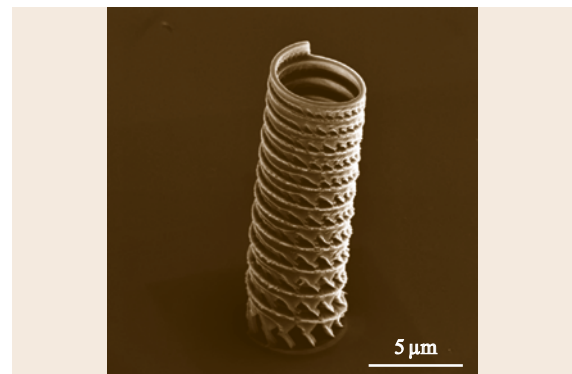

2.75 μm

Fig. 7.3 Micro wine glass with an external diameter of 2.75 μm and a height of 12 μm on a human hair

5 μm

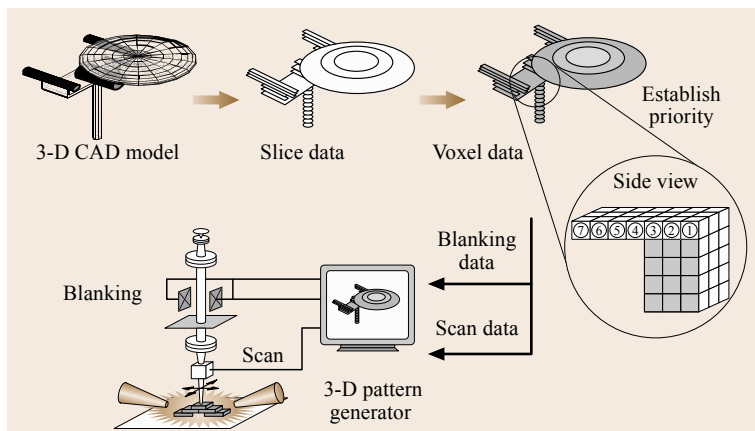**Fig. 7.4** *Micro Leaning Tower of Pisa*

Part A | 7.1

Fig. 7.5 Data flow of 3-D pattern-generating system for FIB-CVD

substrate and on a human hair as works of microstructure plastic art are shown in Figs. 7.2a and 7.3. A micro wine glass with an external diameter of 2.75 μm and a height of 12 μm was formed. The fabrication time was 600 s at a beam current of 16 pA. This beautiful micro wine glass shows the potential of the field of microstructure plastic art. A *micro Colosseum* and a *micro Leaning Tower of Pisa* were also fabricated on a Si substrate, as shown in Figs. 7.2c and 7.4.

Various microsystem parts have been fabricated using FIB-CVD. Figure 7.2b shows a microcoil with a coil diameter of 0.6 μm, a coil pitch of 0.7 μm, and a line width of 0.08 μm. The exposure time was 40 s at a beam current of 0.4 pA. The diameter, pitch, and height of the microcoil were 0.25, 0.20, and 3.8 μm, respectively. The exposure time was 60 s at a beam current of 0.4 pA. The results show that FIB-CVD is a highly promising technique for realizing parts of a microsystem, although their mechanical performance must be measured.

7.1.2 Three-Dimensional Pattern-Generating System

We used ion-beam-assisted deposition of a source gas to fabricate 3-D structures. The 3-D structure is built up as a multilayer structure. In the first step of this 3-D pattern-generating system, a 3-D model of the structure, designed using a 3-D computer-aided design (CAD) system (3-D DXF format), is needed. In this case we realized a structure shaped like a pendulum. The 3-D CAD model, which is a surface model, is cut into several slices, as shown in Fig. 7.5. The thickness of the slices depends upon the resolution in the *z*-direction (the vertical direction). The *x*- and *y*-coordinates of the slices are then used to create the scan data (voxel data). To fabricate the overhanging structure, the ion beam must irradiate the correct positions in the correct order. If the ion beam irradiates a voxel located in mid-air without a support layer, the ions intended for the voxel will be deposited on the substrate. Therefore,
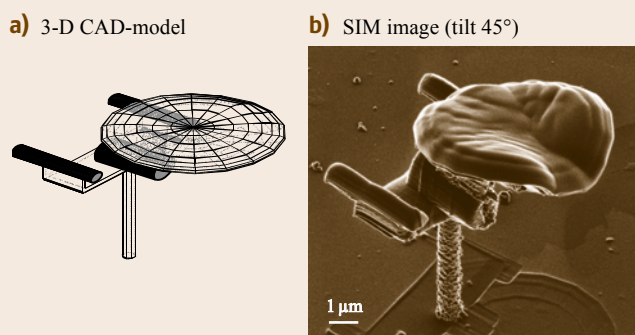

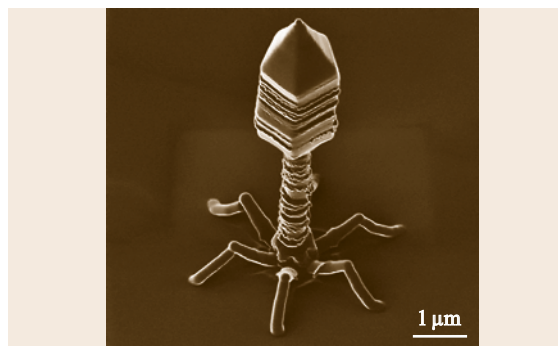**Fig. 7.6a,b** *Micro Starship Enterprise* NCC-1701D, 8.8 μm long

Fig. 7.7 T-4 bacteriophage

the sequence of irradiation is determined, as shown in Fig. 7.5.

The scan data and blanking signal therefore include the scan sequence, the dwell time, the interval time, and the irradiation pitch. These parameters are calculated from the beam diameter, xy-resolution, and z-resolution of fabrication. The z-resolution is proportional to the dwell time and inversely proportional to the square of the irradiation pitch. The scan data are passed to the beam deflector of the FIB-CVD, as are the blanking data. The blanking signal controls the dwell time and interval time of the ion beam.

Figure 7.6 shows a 3-D CAD model and an scanning ion microscope (SIM) image of the star-ship Enterprise NCC-1701D (from the television series Star Trek), which was fabricated by FIB-CVD at $10 \sim 20$ pA [7.8]. The nanospaceship is $8.8\,\mu m$ long and was realized at about $1:100\,000\,000$ scale on silicon substrate. The dwell time (t_d), interval time (t_i), irradiation pitch (p), and total process time (t_p), were $80\,\mu s$, $150\,\mu s$, 2.4 nm, and 2.5 h, respectively. The horizontal overhang structure was successfully fabricated.

Figure 7.7 shows a nano T4 bacteriophage, which is an artificial version of the virus fabricated by FIB-CVD on silicon surface. The size of the artificial nano T4 bacteriophage is about ten times that of the real virus.

7.2 Nanoelectromechanics

7.2.1 Measuring Young's Modulus

An evaluation of the mechanical characteristics of such nanostructures is needed for material physics. *Buks* and *Roukes* reported a simple but useful technique [7.9] for measuring the resonant frequencies of nanoscale objects using a scanning electron microscope (SEM). The secondary electron detector in the SEM can detect frequencies up to around 4 MHz, so the sample vibration is measured as the oscillatory output signal of the detector. *Buks* and *Roukes* used this technique to evaluate the Casimir attractive force between two parallel beams fabricated on a nanoscale. We evaluated the mechanical characteristics of DLC pillars in terms of the Young's modulus, determined using resonant vibration and the SEM monitoring technique [7.10, 11].

The system setup for monitoring mechanical vibration is shown in Fig. 7.8b. There were two ways of measuring the pillar vibrations. One is active measurement, where the mechanical vibration is induced by a thin piezoelectric device, $300\,\mu m$ thick and 3 mm square. The piezo device was bonded to the sidewall of the SEM's sample holder with silver paste. The sample holder was designed to observe cross sections in the SEM (S5000, Hitachi) system. Therefore, the pillar's vibration was observed as a side-view image, as shown in Fig. 7.8a. The range of vibration frequencies involved was 10 kHz up to 2 MHz, which is much faster
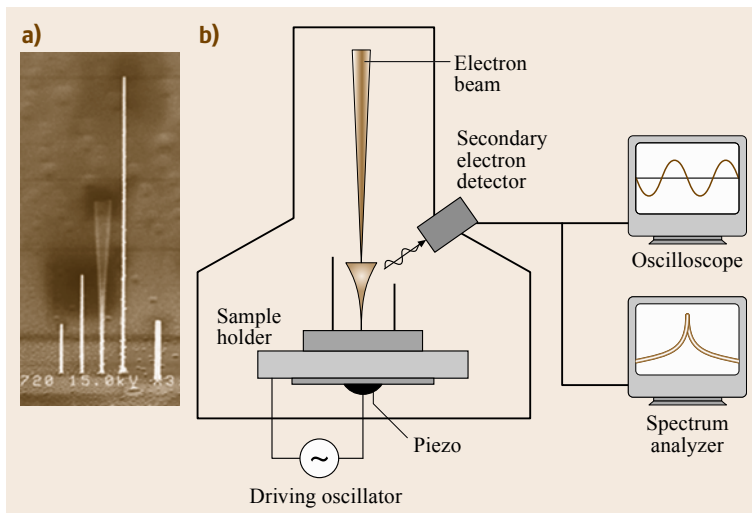

Fig. 7.8 (a) SEM image of the vibration. The resonant frequency was 1.21 MHz. **(b)** Schematic diagram of the vibration monitoring system

than the SEM raster scanning speed. Thus the resonant vibrations of the pillars can be taken as the trace of the pillar's vibration in the SEM image. The resonant frequency and amplitude were controlled by adjusting the power of the driving oscillator.

The other way to measure pillar vibrations is passive measurement using a spectrum analyzer (Agilent 4395A), where most of the vibration seemed to derive from environmental noise from rotary pumps and air conditioners. Some parts of the vibration result from spontaneous vibration associated with thermal excitations [7.9]. Because of the excitation and residual noise, the pillars on the SEM sample holder always vibrated at a fundamental frequency, even if noise isolation is enforced on the SEM system. The amplitude of these spontaneous vibrations was on the order of a few nanometers at the top of the pillar, and high-resolution SEM can easily detect it at a magnification of 300 000.

We arranged several pillars with varying diameters and lengths. The DLC pillars with the smallest diameter of 80 nm were grown using point irradiation. While we used two FIB systems for pillar fabrication, slight differences in the beam diameters of the two systems did not affect the diameters of the pillars. Larger-diameter pillars were fabricated using an area-limited raster scan mode. Raster scanning of a 160 nm^2 region produced a pillar with a cross section of about 240 nm^2, and a 400 nm^2 scan resulted in a pillar with a cross section of 480 nm^2. A typical SEM image taken during resonance is shown in Fig. 7.8a. The FIB-CVD pillars seemed very durable against mechanical vibration. This kind of measurement usually requires at least 30 min, including spectrum analysis and photo recording, but the pillars still survived without any change in resonance characteristics. This durability of the DLC pillars should be useful in nanomechanical applications.

The resonant frequency f of the pillar is defined by (7.1) for a pillar with a square cross section, and (7.2) for a circular cross section

$$f_{\text{square}} = \frac{a\beta^2}{2\pi L^2}\sqrt{\frac{E}{12\rho}} , \tag{7.1}$$

$$f_{\text{circular}} = \frac{a\beta^2}{2\pi L^2}\sqrt{\frac{E}{16\rho}} , \tag{7.2}$$

where a is the width of the square pillar or the diameter of the circular-shaped pillar, L is the length of the pillar, ρ is the density, and E is the Young's modulus. The coefficient β defines the resonant mode; $\beta = 1.875$ for the fundamental mode. We used (7.1) for pillars 240 and 480 nm wide, and (7.2) for pillars grown by point-beam

irradiation. The relationship of the resonant frequency to the Young's modulus, which depends on the ratio of the pillar diameter to the squared length, is summarized in Fig. 7.9. All of the pillars evaluated in this figure were fabricated using the SMI9200 FIB system under rapid growth conditions. Typical growth rates were about 3–5 μm/min for the 100 nm-diameter and 240 μm-wide pillars, and 0.9 μm/min for the 480 nm-wide pillars. When calculating the data shown in Fig. 7.9, we assumed that the density of the DLC pillars was about 2.3 g/cm^3, which is almost identical to that of graphite and quartz. The slope of the line in Fig. 7.9 indicates the Young's modulus for each pillar. The Young's moduli of the pillars were distributed over a range from 65 to 140 GPa, which is almost identical to that of normal metals. Wider pillars tended to have larger Young's moduli.

We found that the stiffness increases significantly as the local gas pressure decreases, as shown in Fig. 7.10. While the absolute value of the local gas pressure at the beam point is very difficult to determine, we found that the growth rate can be a useful parameter for describing the dependence of Young's modulus on pressure. All data points indicated in Fig. 7.10 were obtained from pillars grown using point irradiation. Therefore, the pillar diameters did vary slightly from 100 nm but not by more than 5%. A relatively low gas pressure, with good uniformity, was obtained by using a single gas nozzle and gas reflector. We used a cleaved side-wall of an Si tip as the gas reflector, which was placed 10–50 μm away from the beam point so as to face the gas nozzle. The growth rate was controlled by changing the distance to the wall. While there is a large distribu-
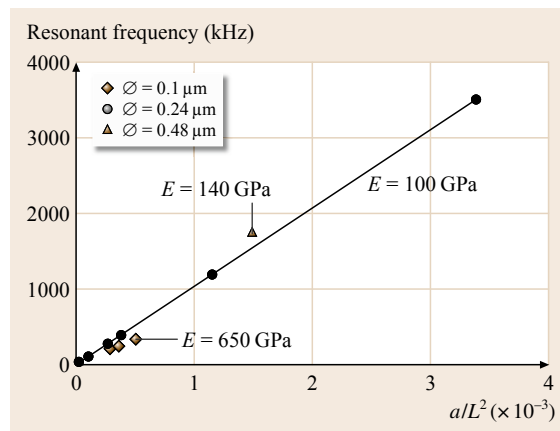

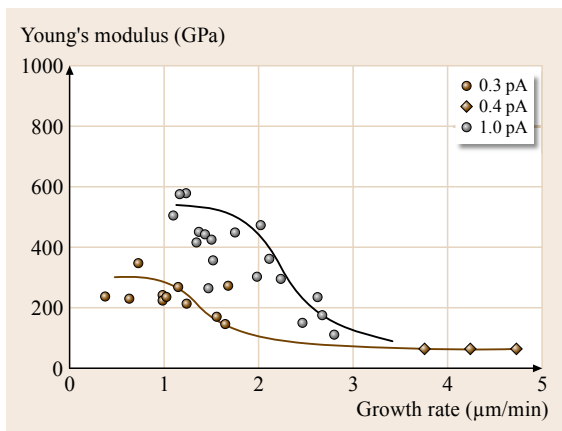**Fig. 7.9** Dependence of resonant frequency on pillar length

Fig. 7.10 Dependence of Young's modulus on growth rate

tion of data points, the stiffness of the pillar tended to become stiffer as the growth rate decreased. The two curves in Fig. 7.10 represent data points obtained for a beam current of 0.3 and 1 pA, respectively. Both curves show the same tendency; the saturated upper levels of the Young's modulus are different for each ion current at low gas pressure (low growth rate). It should be noted that some of the pillars' Young's moduli exceeded 600 GPa, which is of the same order as that of tungsten carbide. In addition, these estimations assume a pillar density of 2.3 g/cm^3, but a finite amount of Ga was incorporated with the pillar growth. If the calculation takes the increase in pillar density due to the Ga concentration into account, the Young's modulus exceeds 800 GPa. Such a high Young's modulus reaches that of carbon nanotubes and natural diamond crystals. We think that this high Young's modulus is due to surface modification caused by the direct ion impact.

In contrast, when the gas pressure was high enough to achieve a growth rate of more than 3 μm/min, the pillars became soft but the change in the Young's modulus was small. The uniformity of the Young's modulus (as seen in Fig. 7.9) presumably results from the fact that the growth occurred in this insensitive region, where the low levels of source gas limit pillar growth.

7.2.2 Free–Space Nanowiring

All experiments were carried out in a commercially available FIB system (SMI9200: SII NanoTechnology Inc.) using a beam of 30 kV Ga$^+$ ions. The beam was focused to a spot size of 7 nm at a beam current of 0.4 pA, and it was incident perpendicular to the surface. The pattern drawing system (CPG-1000: Crestec Co., Tokyo) was added to the FIB apparatus to draw any patterns. Using the CPG, it is possible to control beam scan parameters such as scanning speed, xy-direction, and blanking of the beam, and so 3-D free space nanowiring can be performed [7.12].

Figure 7.11 illustrates the free-space nanowiring fabrication process using both FIB-CVD and CPG. When *phenanthrene* (C$_{14}$H$_{10}$) gas or tungsten hexacarbonyl (W(CO)$_6$) gas, which is a reactive organic gas, is evaporated from a heated container and injected into the vacuum chamber by a nozzle located 300 μm above the sample surface at an angle of about 45° with respect to surface, the gas density of the C$_{14}$H$_{10}$ or W(CO)$_6$ molecules increases on the substrate near the gas nozzle. The nozzle system creates a local high-pressure region over the surface. The base pressure of the sample chamber is 2×10^{-5} Pa and the chamber pressure upon introducing C$_{14}$H$_{10}$ and W(CO)$_6$ as a source gas was 1×10^{-4} and 1.5×10^{-3} Pa, respectively. If a Ga$^+$
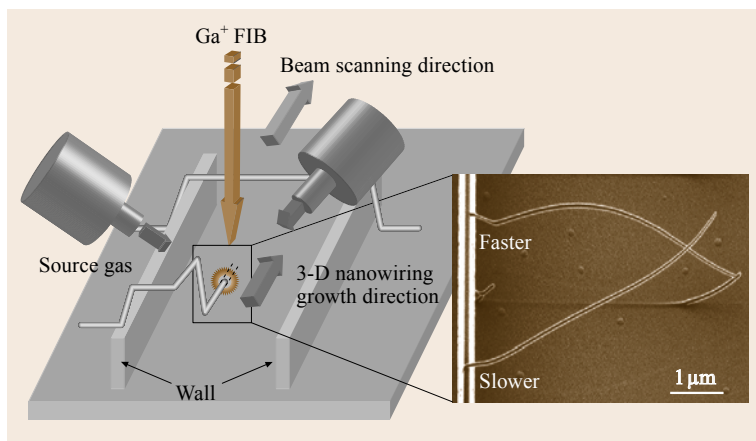
Fig. 7.11 Fabrication of DLC free-space wiring using both FIB-CVD and CPG

ion beam is irradiated onto the substrate, $C_{14}H_{10}$ or $W(CO)_6$ molecules adsorbed on the substrate surface are decomposed, and carbon (C) is mainly deposited onto the surface of the substrate. The direction of deposition growth can be controlling through the scanning direction of the beam. The material deposited using $C_{14}H_{10}$ gas was diamond-like carbon, as confirmed by Raman spectra, and it had a very large Young's modulus of 600 GPa [7.7, 10].

After the two walls shown in Fig. 7.11 were formed, free-space nanowiring was performed by adjusting the beam scanning speed. The ion beam used was a 30 kV Ga^+ FIB, and the irradiation current was 0.8–2.3 pA. The x- and y-scanning directions and the beam scanning speed were controlled by the CPG. The height in the z-direction was proportional to the irradiation time. Deposition is made to occur horizontally by scanning

Fig. 7.12 (a) DLC free-space wiring with a bridge shape. **(b)** DLC free-space wiring with parallel resistances

Fig. 7.13 (a) Radial DLC free-space wiring grown in 16 directions from the center. **(b)** Scanning ion microscope (SIM) micrograph of inductance (L), resistance (R), and capacitor (C) structure

the beam at a certain fixed speed in a plane. However, if the beam scanning speed is faster than the nanowiring growth speed, it grows downward or drops; conversely, if the scanning speed is too slow, the deposition grows slanting upward. Therefore, it is very important to control the beam scanning speed carefully when growing a nanowire horizontally. It turns out that the optimal beam scanning speed to realize a nanowire growing horizontally, using two $C_{14}H_{10}$ gas guns, was about 190 nm/s. The expected pattern resolution archived using FIB-CVD is around 80 nm, because both the primary Ga^+ ion and secondary-electron scattering occur over distances of around 20 nm [7.10, 13].

Figures 7.12 and 7.13 show examples of free-space nanowiring fabricated by FIB-CVD and CPG. All of the structures shown were fabricated using $C_{14}H_{10}$ as a precursor gas.

Figure 7.12a shows nanobridge free-space wiring. The growth time was 1.8 min and the wiring width was 80 nm. Figure 7.12b shows free-space nanowires with parallel resistances. The growth time was 2.8 min, and the wiring width was also 80 nm.

Figure 7.13a shows free-space nanowiring grown in 16 directions from the center. Figure 7.13b shows a scanning ion microscope (SIM) image of an inductor (L), a resistor (R), and a capacitor (C) in a parallel circuit structure with free-space nanowiring. A coiled structure was fabricated by circle-scanning of the Ga^+ FIB. The growth times of the L, R, and C structures were about 6, 2, and 12 min, and all the nanowiring is about 110 nm wide. From these structures, one can see that it is possible to fabricate nanowiring at an arbitrary position using FIB-CVD and CPG. These results also indicate that various circuit structures can be formed by combining L, C, and R.

The free-space wiring structures were observed using 200 keV TEM. The analyzed area was 20 nm in diameter. Figure 7.14a,b shows TEM images of DLC free-space wiring and a pillar. It became clear from these energy-dispersive x-ray (EDX) measurements that the dark part (A) of Fig. 7.14a corresponds to the Ga core, while the outside part (B) of Fig. 7.14a corresponds to amorphous carbon. This free-space wiring therefore consists of amorphous carbon with a Ga core. The center position of the Ga core is actually located below the center of the wiring. However, in the case of the DLC pillar, the Ga core is located at the center of the pillar. To investigate the difference between these core positions, the Ga core distribution in free-space wiring was observed in detail by TEM. The center position of the Ga core was about 70 nm from the top, which was
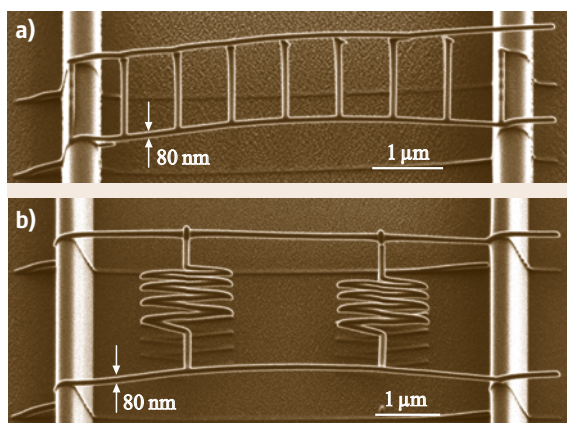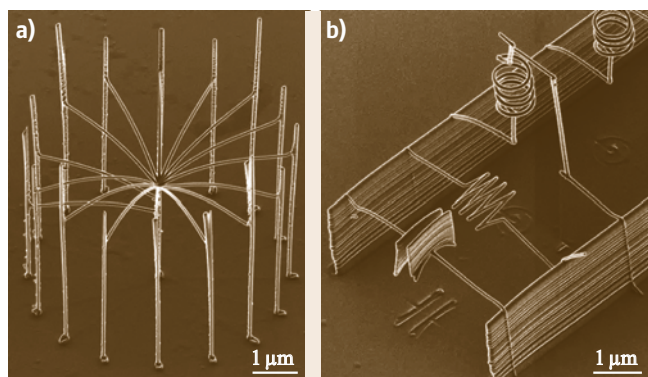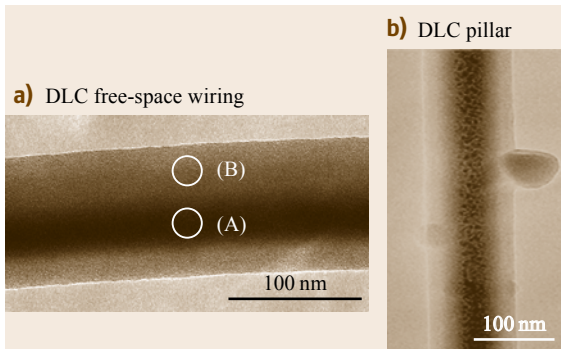
Fig. 7.14a,b TEM images of **(a)** DLC free-space wiring and **(b)** DLC pillar

20 nm below the center of the free-space wiring. We calculated an ion range of 30 kV Ga ions into amorphous carbon, using transport of ions in matter (TRIM), of 20 nm. The calculation indicates that the displacement of the center of the Ga core in the nanowiring corresponds to the ion range.

The electrical properties of free-space nanowiring fabricated by FIB-CVD using a mixture of $C_{14}H_{10}$ and $W(CO)_6$ were measured. Nanowiring was fabricated on an Au electrode. These Au electrodes were formed on a 0.2 μm-thick SiO_2-on-Si substrate by an EB lithography and lift-off process. Two-terminal electrode method was used to measure the electrical resistivity of the nanowiring. Figure 7.15a shows the results for nanowiring fabricated using only $C_{14}H_{10}$ source gas. The growth time here was 65 s and the wiring width was 100 nm. Next, $W(CO)_6$ gas was added to the $C_{14}H_{10}$ gas to create a gas mixture containing a metal in order to obtain lower electrical resistivity. Figure 7.15b–d corresponds to increasing $W(CO)_6$ contents in the gas mixture. The $W(CO)_6$ content rate was controlled by the sublimation temperature of the $C_{14}H_{10}$ gas. As the $W(CO)_6$ content was increased, the nanowiring growth time and width become longer, being 195 s and 120 nm for Fig. 7.15b, 237 s and 130 nm for Fig. 7.15c, and 296 s and 140 nm for Fig. 7.15d. Finally, we tried to fabricate free-space nanowiring using only $W(CO)_6$, but did not obtain continuous wiring, because the deposition rate for a source gas of just $W(CO)_6$ was very slow.

The electrical resistivity (Fig. 7.15a) for nanowiring fabricated using only $C_{14}H_{10}$ source gas was $1 \times 10^2 \, \Omega$ cm. The elemental contents were 90% C and 10% Ga, as measured using a SEM-EDX spot beam. The $I–V$ curves in Fig. 7.15b–d correspond to increasing $W(CO)_6$ content in the gas mixture. As the $W(CO)_6$ content increases, the electrical resistivity decreases,

as shown in the $I–V$ curves (Fig. 7.15b–d). Moreover, the Ga content also increased because the growth of nanowiring slowed; the irradiation time of the Ga^+ FIB became longer. The electrical resistivities calculated from the $I–V$ curves (Fig. 7.15b–d) were 16×10^{-2}, 4×10^{-2}, and $2 \times 10^{-2} \, \Omega$ cm, respectively. The electrical resistivity in Fig. 7.15e, which was fabricated by using only $W(CO)_6$ source gas, was $4 \times 10^{-4} \, \Omega$ cm. Increasing the Ga and W metallic content decreases the electrical resistivity, as shown by the SEM-EDX measurements reported in Fig. 7.15. These results indicate that increasing metallic content results in lower resistivity.

Electron holography is a useful technology for direct observation of electrical and magnetic fields at the nanoscale, and also has the property of showing useful information by detecting the phase shift of the electron wave due to the electrical and magnetic field. The technique relies upon an electron biprism, which plays the important role of dividing the electron wave into a reference wave and an objective wave. The biprism is composed of one thin filament and two ground electrodes.

It is important to fabricate as narrow a filament as possible to obtain an interference fringe with high contrast and good fringe quality. However, fabricating the filament with a diameter below 500 nm is very difficult, because a conventional electron biprism is fabricated by pulling a melted glass rod by hand. To overcome this problem, we introduce a new fabrication technique for
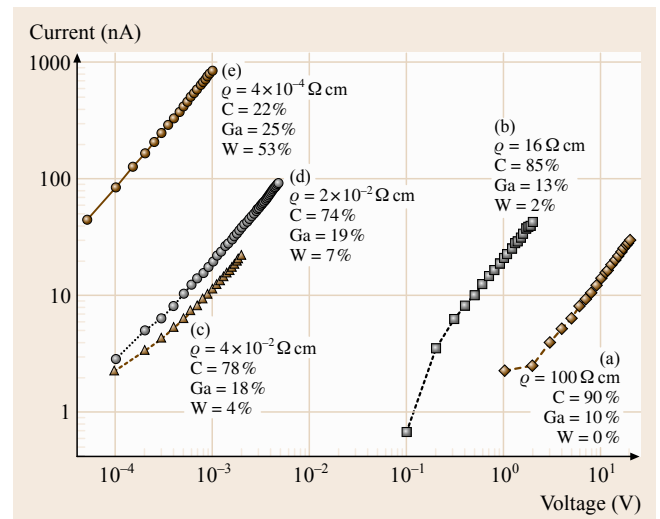
Fig. 7.15 Electrical resistivity measurement for nanowiring. The electrical resistivity ρ was calculated from the $I–V$ curve. Elemental contents of C, Ga, and W were measured by SEM-EDX

Fig. 7.16 Electron biprism fabricated by FIB-CVD

the electron biprism using FIB-CVD, and evaluate the characteristics of the new biprism [7.14].

Figure 7.16 shows an SEM micrograph of the FIB-CVD biprism. We successfully fabricated DLC wiring with a smooth surface in between W rods by free-space wiring fabrication based on FIB-CVD technology. The 80 nm DLC thin wiring works as the filament of the biprism. The diameter and length of the filament are 80 nm and 15 μm, respectively.

Figure 7.17 shows interference fringes obtained using the biprism with a filament of 80 nm diameter (Fig. 7.17a) and 400 nm diameter (Fig. 7.17b), and cor-

responding fringe profiles. The applied prism voltage was 20 V, respectively. The filament with 400 nm diameter, close to the standard size used in the conventional electron biprism, was fabricated by Pt sputter-coating onto the 80 nm-diameter filament. Interference fringes were successfully obtained. Moreover, the interference region of the fringe obtained using the biprism with the 80 nm-diameter filament is larger than that of the fringe obtained using the biprism with the 400 nm-diameter filament. These results demonstrate the adequacy of the thin filament fabricated by FIB-CVD, and the new biprism will be very useful for accurate observation with high contrast and good fringe quality in electron holography.

7.2.3 Nanomechanical Switch

We have also demonstrated a nanomechanical switch fabricated by FIB-CVD [7.15]. Figure 7.18a shows the principle behind the realization of a nanomechanical switch. First, an Au electrode was formed on
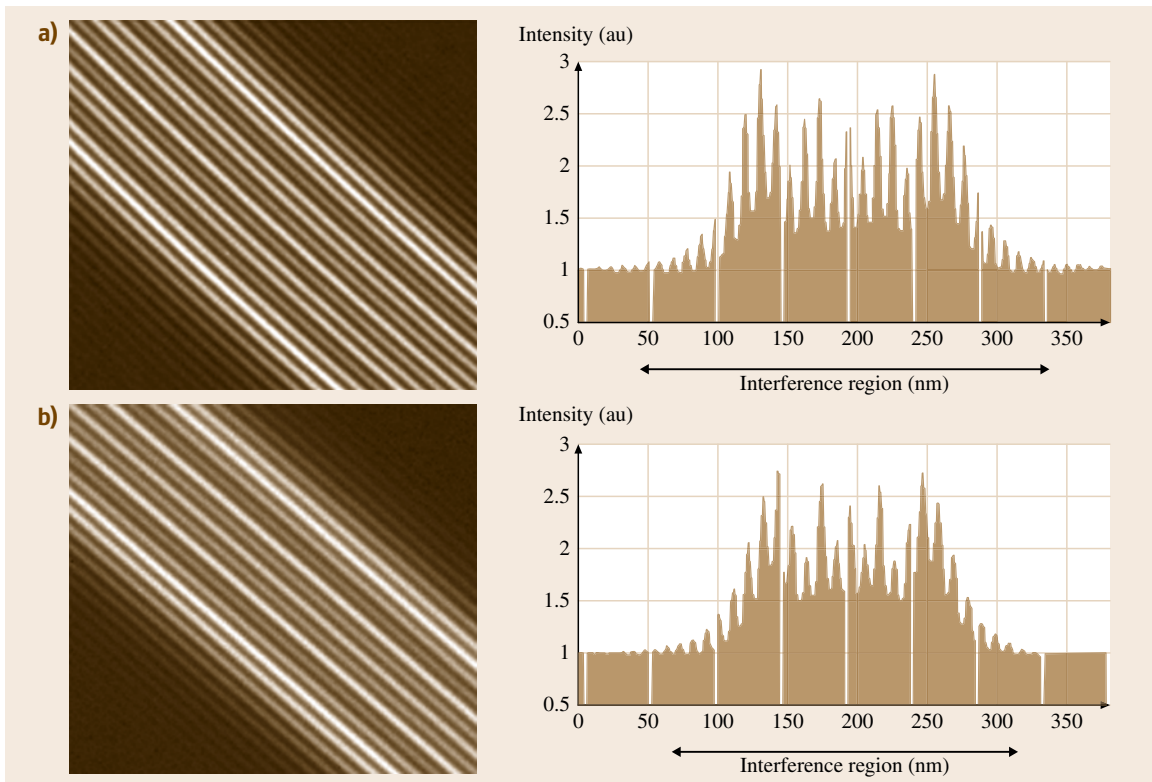

Fig. 7.17a,b Interference fringes and corresponding fringe profiles. (**a**) Obtained using the biprism with diameter of 80 nm, and (**b**) obtained using the biprism with diameter of 400 nm

a 0.2 μm-thick SiO_2-on-Si substrate by an electron-beam lithography and lift-off process. After that, a coil and free-space nanowiring were fabricated onto the Au electrode to form a switch function using nanowiring fabrication technology with FIB-CVD and CPG. The coil structure was fabricated by scanning a Ga^+ beam in a circle at fixed speed in $C_{14}H_{10}$ ambiance gas. An electric charge (positive or negative) was applied to the coil, and the reverse electric charge was applied to the nanowiring. The coil extended upward when a voltage was applied, because these was now an electrical repulsive force between each loop of the coil. At the same time, the coil and the nanowiring gravitated toward one another, because they had opposite charges. This attraction caused the coil to contact with the nanowiring when a certain threshold voltage was reached.

Next, we evaluated the switch function by measuring the current that flowed when the coil and the nanowiring were in contact. Figure 7.18b,c shows SIM micrographs of the nanomechanical switch before and after applying a voltage. These micrographs indicate that the coil and nanowiring make contact when a voltage is applied to the coil. At the same time, $I-V$ measurements of the nanomechanical switch were carried out, as shown in Fig. 7.19a. The current was plotted against the applied voltage at room temperature, and from this graph, it was apparent that the current begins to flow at a threshold voltage of 17.6 V. At this point, the electrical resistance and the resistivity of the nanomechanical switch are about 250 MΩ and 11 Ω cm, respectively. We measured the $I-V$ characteristics for ten nanomechanical switches. The threshold voltage was around 20 V in each case. The switching function was confirmed by performing on/off operations at an ap-
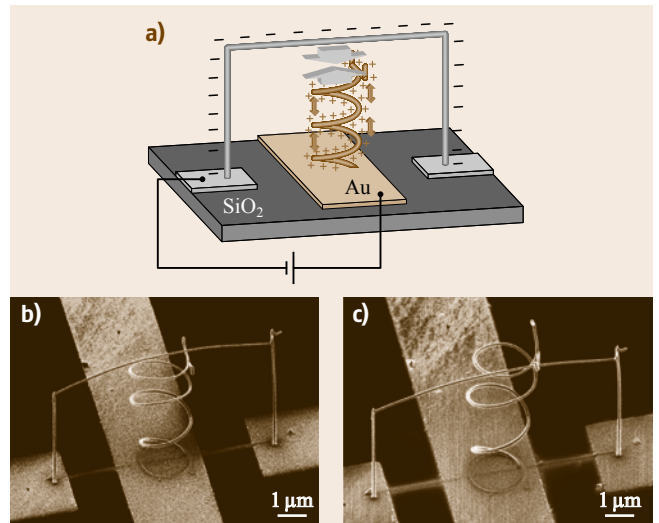
Fig. 7.18 (a) Principle of movement of nanomechanical switch. SIM micrographs of nanomechanical switch: **(b)** before applying voltage and **(c)** after applying voltage

plied voltage of 30 V, as shown in Fig. 7.19b. A pulsed current of about 170 nA was detected for this applied voltage.

7.2.4 Nanoelectrostatic Actuator

The fabrication process of 3-D nanoelectrostatic actuators (and manipulators) is very simple [7.16]. Figure 7.20 shows the fabrication process. First, a glass capillary (GD-1: Narishige Co., East meadow, NY) was pulled using a micropipette puller (PC-10: Narishige Co.). The dimensions of the glass capillary were 90 mm in length and 1 mm in diameter. Using this process,
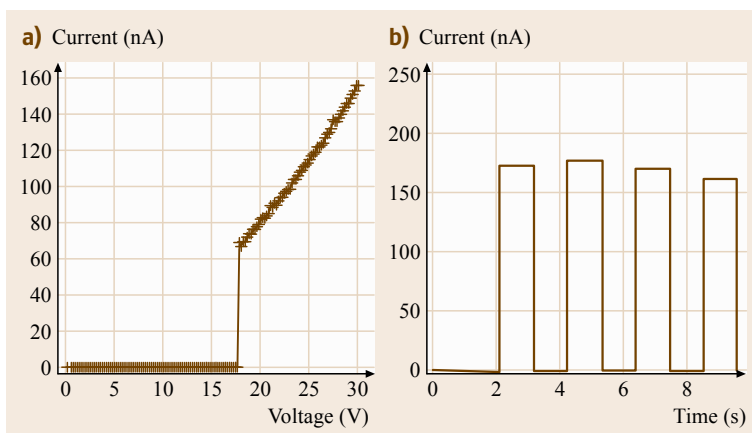
Fig. 7.19 (a) $I-V$ curve for the nanomechanical switch. **(b)** Pulsed current to on/off operation for the nanomechanical switch at an applied voltage of 30 V
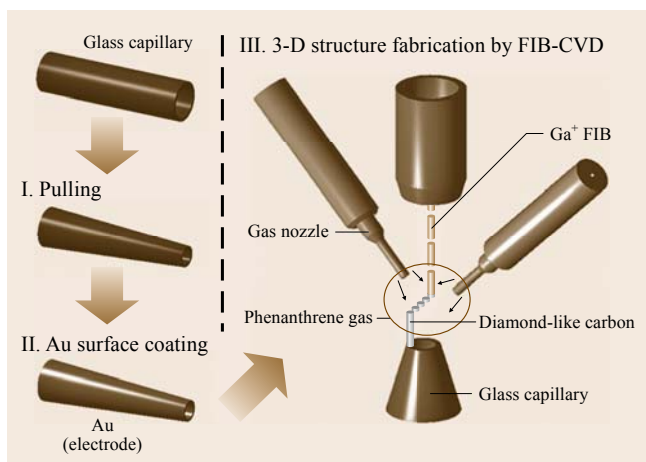
Fig. 7.20 Fabrication process of 3-D nanoelectrostatic actuators

we obtained a glass capillary tip with a 1 μm diameter. Next, we coated the glass capillary surface with Au by direct-current (DC) sputtering. The Au thickness was ≈ 30 nm. This Au coating serves as the electrode that controls the actuator and manipulator. Then, the 3-D nanoelectrostatic actuators and manipulators were fabricated by FIB-CVD. This process was carried out in a commercially available FIB system (SIM9200: SII NanoTechnology Inc.) with a Ga^+ ion beam operating at 30 keV. FIB-CVD was carried out using a *phenanthrene* ($C_{14}H_{10}$) precursor as the source material. The beam diameter was about 7 nm. The inner diameter of each nozzle was 0.3 mm. The *phenanthrene* gas pressure during growth was typically 5×10^{-5} Pa in the specimen chamber. The Ga^+ ion beam was controlled by transmitting CAD data on the arbitrary structures to the FIB system.

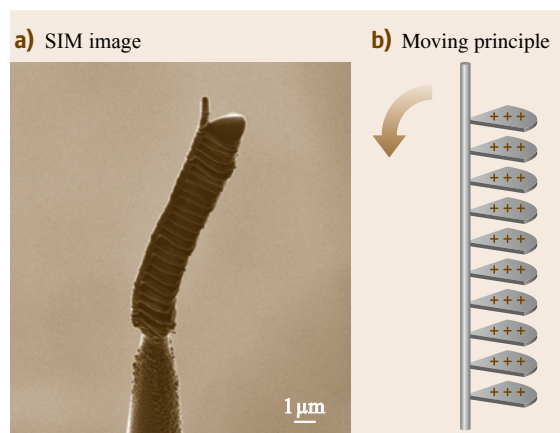**Fig. 7.22** Dependence of bending distance on applied voltage

Fig. 7.21a,b Laminated pleats-type electrostatic actuator. **(a)** SIM image of a laminated pleats-type electrostatic actuator fabricated on the tip of a Au-coated glass capillary. **(b)** Illustration of moving principle of the actuator

A laminated pleats-type electrostatic actuator was fabricated by FIB-CVD. Figure 7.21a shows an SIM image of a laminated pleats-type electrostatic actuator fabricated at 7 pA and 60 min exposure time. Figure 7.21b shows the principle behind the movement of this actuator. The driving force is the repulsive force due to the accumulation of electric charge. This electric charge can be stored in the pleats structures of the actuator by applying a voltage across the glass capillary. The pillar structure of this actuator bends due to charge repulsion, as shown in Fig. 7.21b. Figure 7.22 shows the dependence of the bending distance on the
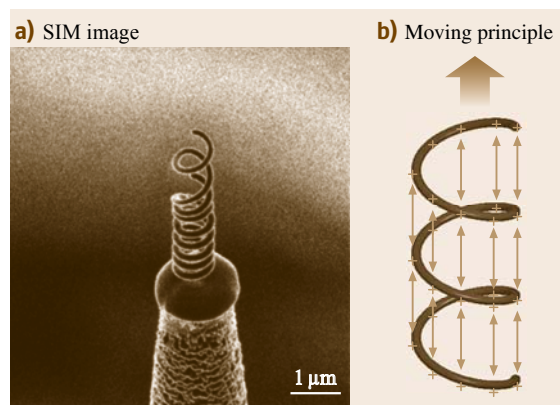

Fig. 7.23a,b Coil-type electrostatic actuator. **(a)** SIM image of a coil-type electrostatic actuator fabricated on the tip of a Au-coated glass capillary. **(b)** Illustration of moving principle for the actuator
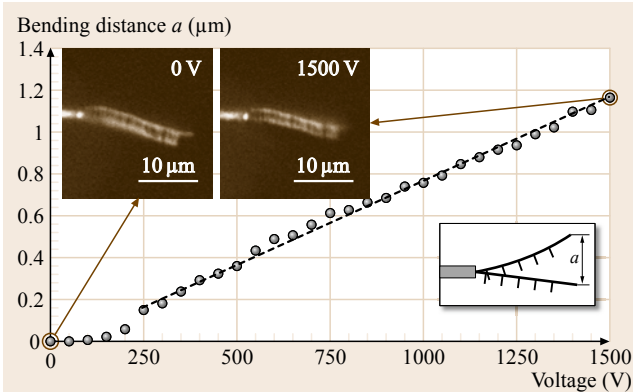
applied voltage. The bending distance is defined as the distance *a* in the inset of Fig. 7.22. The bending rate of this laminated pleats-type electrostatic actuator was about 0.7 nm/V.

A coil-type electrostatic actuator was fabricated by FIB-CVD. Figure 7.23a shows an SIM image of a coil-type electrostatic actuator fabricated at 7 pA and 10 min of exposure time. Figure 7.23b shows the principle behind the movement of this actuator, which is very simple. The driving force is the repulsive force induced by electric charge accumulation; the electric charge can be stored in this coil structure by applying a voltage across the glass capillary. This coil structure expands and contracts due to charge repulsion, as shown in Fig. 7.23b. Figure 7.24 shows the dependence of the coil expansion on the applied voltage. The length of the expansion is the distance *a* in the inset of Fig. 7.24. The result revealed that the expansion could
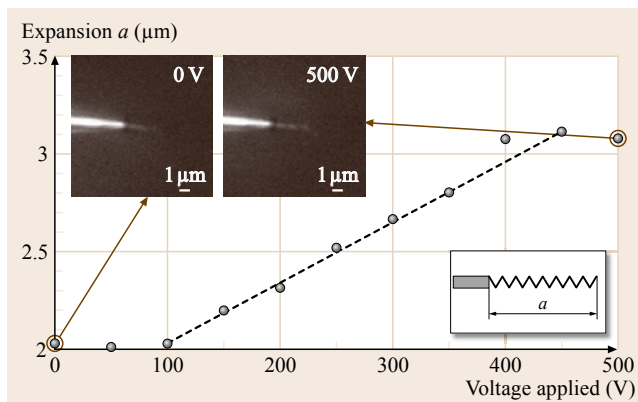

Fig. 7.24 Dependence of coil expansion on applied voltage

be controlled in the applied voltage range from 0 to 500 V.

7.3 Nanooptics: Brilliant Blue Observation from a *Morpho* Butterfly Scale Quasistructure

The *Morpho* butterfly has brilliant blue wings, and the source of this intense color has been an interesting topic of debate for a long time. Due to an intriguing optical phenomenon, the scales reflect interfered brilliant blue color for any angle of incidence of white light. This color is called a structural color, meaning that it is not caused by pigment reflection [7.17]. When we observed the scales with a scanning electron microscope (SEM) (Fig. 7.25a), we found three-dimensional (3-D) nanostructures 2 μm in height, 0.7 μm in width, and with a 0.22 μm grating pitch on the scales. These nanostructures cause a similar optical phenomenon to the iridescence produced by a jewel beetle.

We duplicated the *Morpho* butterfly scale quasistructure with a commercially available FIB system (SMI9200: SII Nanotechnology Inc.) using a Ga$^+$ ion beam operating at 30 kV [7.18]. The beam diameter was about 7 nm at 0.4 pA. The FIB-CVD was performed using *phenanthrene* ($C_{14}H_{10}$) as a precursor.

In this experiment, we used a computer-controlled pattern generator, which converted 3-D computer-aided design (CAD) data into a scanning signal, which was passed to an FIB scanning apparatus in order to fabricate a 3-D mold [7.8]. The scattering range of the Ga primary ions is about 20 nm, and the range of the secondary electrons induced by the Ga ion beam is about

20 nm, so the expected pattern resolution of the FIB-CVD is about 80 nm.

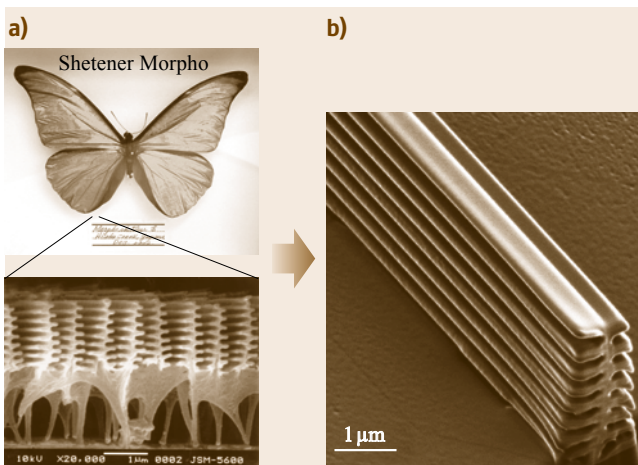Figure 7.25b shows an SIM image of the *Morpho* butterfly quasistructure fabricated by FIB-CVD using 3-

Fig. 7.25a,b *Morpho* butterfly scales. (**a**) Optical microscope image showing top view of *Morpho* butterfly. SEM image showing a cross-sectional view of *Morpho* butterfly scales. (**b**) SIM image showing inclined view of *Morpho* butterfly scale quasistructure fabricated by FIB-CVD

Part A | 7.3

D CAD data. This result demonstrates that FIB-CVD can be used to fabricate the quasistructure.

We measured the reflection intensities from *Morpho* butterfly scales and the *Morpho* butterfly scale quasistructure optically; white light from a halogen lamp was directed onto a sample with angles of incidence ranging from 5° to 45°. The reflection was concentrated by an optical microscope and analyzed using a commercially available photonic multichannel spectral analyzer system (PMA-11: Hamamatsu Photonics K.K., Hamamatsu City, Japan). The intensity of light incident from the halogen lamp had a peak at a wavelength close to 630 nm.

The *Morpho* butterfly scale quasistructure was made of DLC. The reflectivity and transmittance of a 200 nm-thick DLC film deposited by FIB-CVD, measured by the optical measurement system at a wavelength close to 440 nm (the reflection peak wavelength of the *Morpho* butterfly), were 30% and 60%, respectively. Therefore, the measured data indicated that the DLC film had high reflectivity near 440 nm, which is important for the fabrication of an accurate *Morpho* butterfly scale quasistructure.

We measured the reflection intensities of the *Morpho* butterfly scales and the quasistructure with an optical measurement system, and compared their characteristics. Figure 7.26a,b shows the reflection intensities from *Morpho* butterfly scales and the quasistructure, respectively. Both gave a peak intensity near 440 nm and showed very similar reflection intensity spectra for various angles of incidence.

We have thus successfully demonstrated that a *Morpho* butterfly scale quasistructure fabricated using
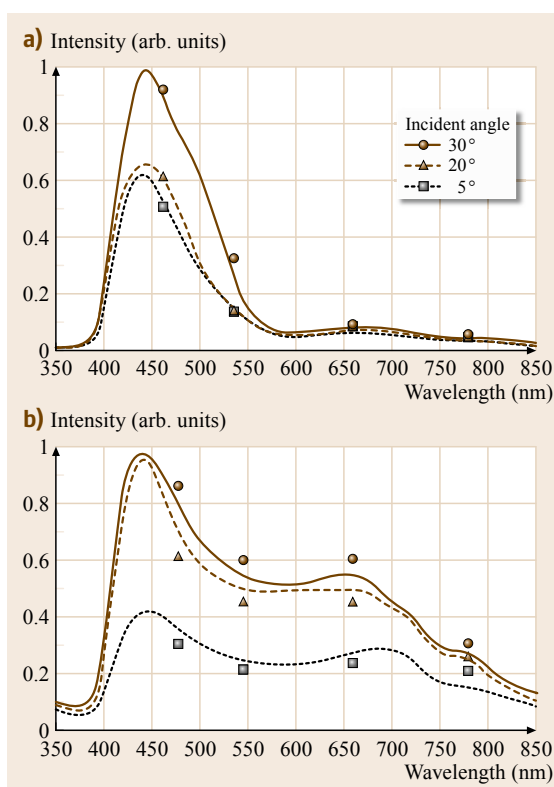

Fig. 7.26a,b Intensity curves of the reflection spectra for: **(a)** *Morpho* butterfly scales, **(b)** *Morpho* butterfly scale quasistructure

FIB-CVD can give almost the same optical characteristics as real *Morpho* butterfly scales.

7.4 Nanobiology

7.4.1 Nanoinjector

Three-dimensional nanostructures on a glass capillary have a number of useful applications, such as manipulators and sensors in various microstructures. We have demonstrated the fabrication of a nozzle nanostructure on a glass capillary for a bioinjector using 30 keV Ga^+ focused ion beam assisted deposition with a precursor of phenanthrene vapor and etching [7.19]. It has been demonstrated that nozzle nanostructures of various shapes and sizes can be successfully fabricated. An inner tip diameter of 30 nm on a glass capillary and a tip shape with an inclined angle have been realized. We re-

ported that diamond-like carbon (DLC) pillars grown by FIB-CVD with a precursor of *phenanthrene* vapor have very large Young's moduli, exceeding 600 GPa, which potentially makes them useful for various applications [7.10]. These characteristics are applicable to the fabrication of various biological devices.

In one experiment, nozzle nanostructure fabrication for biological nanoinjector research was studied. The tip diameters of conventional bioinjectors are greater than 100 nm and the tip shapes cannot be controlled. A bio-nanoinjector with various nanostructures on the top of a glass capillary has the following potential applications (shown in Fig. 7.27):
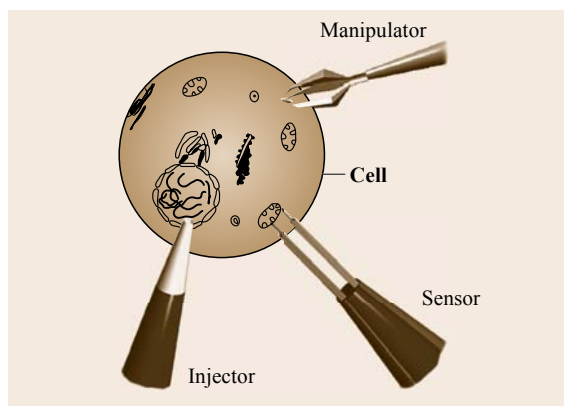
Fig. 7.27 Potential uses for a bionanoinjector

1. Injection of various reagents into a specific organelle in a cell
2. Selective manipulation of a specific organelle outside of a cell by using the nanoinjector as an aspirator
3. Reducing the mechanical stress produced when operating in the cell by controlling the shape and size of the bionanoinjector
4. Measurement of the electric potential of a cell, an organelle, and an ion channel exiting on a membrane, by fabricating an electrode

Thus far, 3-D nanostructure fabrications on a glass capillary have not been reported. We present nozzle nanostructure fabrication on a glass capillary by FIB-CVD and etching in order to confirm the possibility of bionanoinjector fabrication.

The nozzle structures of the nanoinjector were fabricated using a function generator (Wave Factory: NF Electronic Instruments, Yokohama, Japan). Conventional microinjectors are fabricated by pulling a glass capillary (GD-1: Narishige Co.) using a micropipette puller (PC-10: Narishige Co.). The glass capillary was 90 mm in length and 1 mm in diameter.

Conventionally, the tip shape of a microinjector made by pulling a glass capillary, and which is used as an injector into a cell, is controlled by applying mechanical grinding (or not). However, the reliability of this technique for controlling tip shape is very poor and requires experienced workers.

A bionanoinjector tip was fabricated on a glass capillary by FIB-CVD, as shown in Fig. 7.28a–c. First, FIB etching made the tip surface of the glass capillary smooth. Then, a nozzle structure was fabricated at the tip by FIB-CVD. Figure 7.28a shows the surface of a chip smoothed at 120 pA and after 30 s exposure time by FIB etching, with inner hole diameter of 870 nm. A nozzle structure fabricated by FIB-CVD with inner hole diameter of 220 nm is shown in Fig. 7.28b. Figure 7.28c shows a cross section of Fig. 7.28b. These results demonstrate that a bionanoinjector could be successfully fabricated by 3-D nanostructure fabrication using FIB-CVD. The bionanoinjector was used to inject dye into a egg cell (*Ciona intestinalis*) as shown in Fig. 7.29.

7.4.2 Nanomanipulator

An electrostatic 3-D nanomanipulator that can manipulate nanoparts and operate on cells has been developed by FIB-CVD. This 3-D nanomanipulator has four fingers so that it can manipulate a variety of shapes. To move the nanomanipulator, electric charge is accumulated in the structure by applying voltage to the four-fingered structure, and electric charge repulsion causes them to move. Furthermore, we succeeded in catching a microsphere (made from polystyrene latex) with a diameter of 1 μm using this 3-D nanomanipulator with four fingers [7.20].

The glass capillary (GD-1; Narishige Co.) was pulled using a micropipette puller (PC-10; Narishige Co.). A tip diameter of about 1.0 μm could be obtained using this process. Then, the glass capillary surface was coated with Au in order to fabricate an electrode for
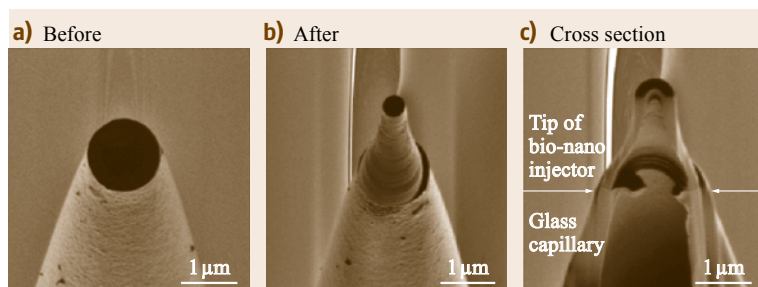
Part A | 7.4

a) Before   b) After   c) Cross section

Tip of bio-nano injector

Glass capillary

1 μm

Fig. 7.28a–c SIM images of a bionanoinjector fabricated on a glass capillary by FIB-CVD. **(a)** Before FIB-CVD, **(b)** after FIB-CVD, and **(c)** cross section of **(b)**
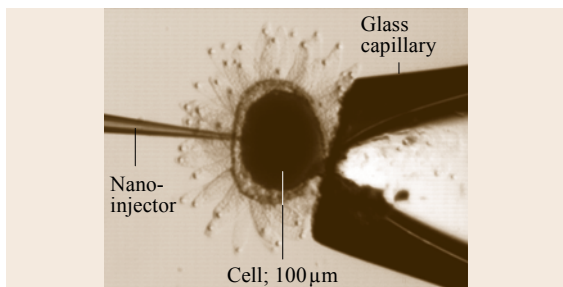
Fig. 7.29 Injection into an egg cell (*Ciona intestinalis*) using a bionanoinjector

nanomanipulator control. The thickness of the Au coating was about 30 nm. Finally, a 3-D nanomanipulator structure with four fingers (Fig. 7.30) was fabricated by FIB-CVD on the tip of the glass capillary with an electrode.

Microsphere (a polystyrene latex ball with a diameter of 1 μm) manipulation was carried out using the 3-D nanomanipulator with four fingers. An illustration of this manipulation experiment is shown in Fig. 7.31. By connecting the manipulator fabricated by FIB-CVD to a commercial manipulator (MHW-3; Narishige Co.), the direction of movement along the *x*-, *y*-, and *z*-axis could be controlled. The microsphere target was fixed to the side of a glass capillary, and the manipulation was observed from the top with an optical microscope.

The optical microscope image of Fig. 7.32 shows the situation during manipulation. First, the 3-D nanomanipulator was made to approach the microsphere; no voltage was applied. Next, the four fingers were opened by applying 600 V in front of the microsphere and the microsphere could be caught by turning off the voltage when the microsphere was in the grasp of the nanomanipulator. The 3-D nanomanipulator was then removed from the side of the glass capillary. Note
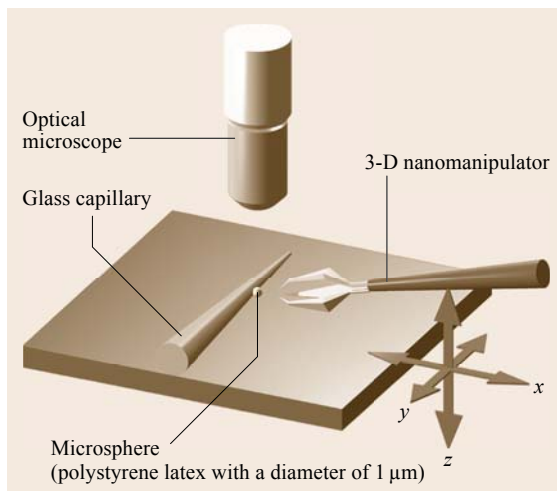

Fig. 7.31 Illustration of 1 μm polystyrene microsphere manipulation by using a 3-D electrostatic nanomanipulator with four fingers
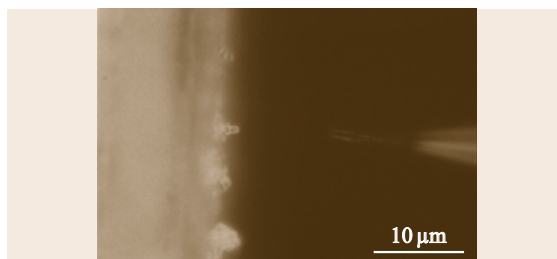

Fig. 7.32 In situ observation of 1 μm polystyrene microsphere manipulation using a 3-D electrostatic nanomanipulator with four fingers
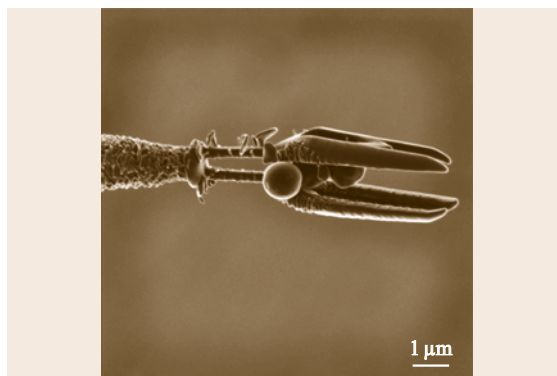

Fig. 7.33 SIM image of the 3-D electrostatic nanomanipulator with four fingers after manipulation
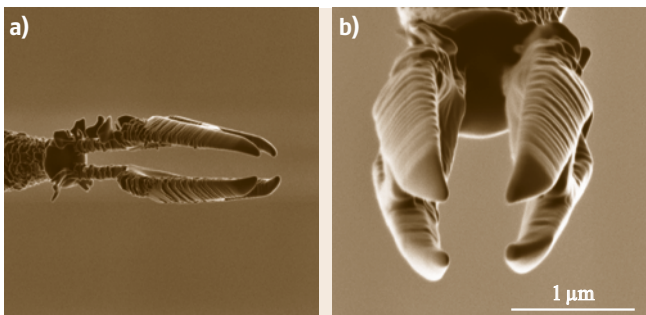

Fig. 7.30a,b SIM image of the 3-D electrostatic nanomanipulator with four fingers before manipulation. **(a)** Side view, **(b)** top view

that the action of catching the microsphere occurs due to the elastic force of the manipulator's structure. We

succeeded in catching the microsphere, as shown in the SIM image in Fig. 7.33.

Nanonet

Highly functional nanotools are required to perform subcellular operations and analysis in nanospace. For example, nanotweezers have been fabricated on an AFM tip from carbon nanotube [7.21]. We have produced nanotools with arbitrary structures using FIB-CVD. Recently, we have fabricated a nanonet as a novel nanotool for the manipulation and analysis of subcellular organelles; subcellular operations like these are easy to perform using a nanonet [7.22].

To realize the nanonet, a glass capillary (GD-1: Narishige Co.) was pulled with a micropipette puller (PC-10: Narishige Co.). The glass capillary was 90 mm in length and 1 mm in diameter. Using this process, we obtained a 1 μm-diameter tip on the glass capillary. Next, the glass capillary's surface was coated with Au for protection during charging with a Ga^+ ion beam. In the final processes, the nanonet structure was fabricated with FIB-CVD. We used a commercially available FIB system (SIM2050MS2: SII NanoTechnology Inc.) that has a Ga^+ ion beam operating at 30 kV. The source material for FIB-CVD was a *phenanthrene* ($C_{14}H_{10}$) precursor. Diamond-like carbon (DLC) is deposited by using this source material. The minimum beam diameter was about 5 nm.

The *phenanthrene* gas pressure in the specimen chamber during growth was typically 5×10^{-5} Pa. By transmitting the CAD data for the arbitrary structures to the FIB system, we were able to control the Ga^+ ion beam, and therefore to fabricate the nanonet structure on the glass capillary.

The flexibility and practicality of the nanonet is enhanced by fabricating it on a glass capillary, since this is used in many fields, including biology and medicine. The FIB-CVD deposition time was about 40 min at a beam current of 7 pA. The diameter of the ring used to hang the net was about 7 μm, and the width of the net was about 300 nm.

We performed an experiment under an optical microscope in which polystyrene microspheres were captured with the nanonet. Figure 7.34 shows a schematic of the experimental apparatus. Polystyrene microspheres with a diameter of 2 μm were dispersed in distilled water to simulate subcellular organelles. The *x*-, *y*-, and *z*-axis movements of the FIB-CVD nanonet
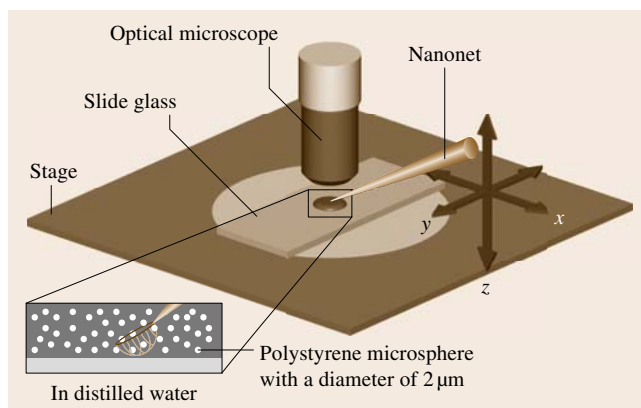

Fig. 7.34 Schematic drawing of the experiment where polystyrene microspheres were captured using a nanonet

were precision-controlled using a commercial manipulator (MHW-3; Narishige Co.).

We performed in situ observations of the capture of 2 μm-diameter polystyrene microspheres using the nanonet. First, the nanonet was brought to the surface of the water. Next, we placed the nanonet into distilled water by controlling its *z*-axis movement with a commercial manipulator. Then the microspheres were scooped up by moving the nanonet upward. Finally, the nanonet was removed from the surface of the water. At this point, the nanonet had scooped up three microspheres. After the in situ experiments, we observed that the nanonet contained the 2 μm-diameter microspheres. Figure 7.35 shows an SIM image of the nanonet holding the captured microspheres. This proves that we successfully captured the microspheres.
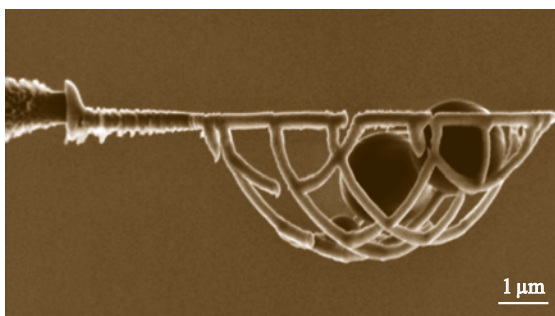

Fig. 7.35 SIM image of nanonet holding three microspheres after capture

7.5 Summary

Three-dimensional nanostructure fabrication using 30 keV Ga$^+$ FIB-CVD and a *phenanthrene* ($C_{14}H_{10}$) source as a precursor has been demonstrated. The film deposited on a silicon substrate was characterized using a transmission microscope and Raman spectra. This characterization indicated that the deposited film is diamond-like amorphous carbon, which has attracted attention due to its hardness, chemical inertness, and optical transparency. Its large Young's modulus, which exceeds 600 GPa, makes it highly desirable for various applications. A nanoelectrostatic actuator and 0.1 μm nanowiring were fabricated and evaluated as parts of nanomechanical system. Furthermore, a nanoinjector and nanomanipulator were fabricated as novel nanotools for manipulation and analysis of subcellular organelles. These results demonstrate that FIB-CVD is one of the key technologies needed to make 3-D nanodevices that can be used in the field of electronics, mechanics, optics, and biology.

References

7.1   S. Matsui: Nanostructure fabrication using electron beam and its application to nanometer devices, Proc. IEEE **85**, 629 (1997)

7.2   O. Lehmann, F. Foulon, M. Stuke: Surface and three-dimensional processing by laser chemical vapor deposition, NATO ASI Ser. Appl. Sci. **265**, 91 (1994)

7.3   H.W. Koops, J. Kretz, M. Rudolph, M. Weber, G. Dahm, K.L. Lee: Characterization and application of materials grown by electron-beam-induced deposition, Jpn. J. Appl. Phys. **33**, 7099 (1994)

7.4   A. Wagner, J.P. Levin, J.L. Mauer, P.G. Blauner, S.J. Kirch, P. Long: X-ray mask repair with focused ion beams, J. Vac. Sci. Technol. B **8**, 1557 (1990)

7.5   I. Utke, P. Hoffmann, B. Dwir, K. Leifer, E. Kapon, P. Doppelt: Focused electron beam induced deposition of gold, J. Vac. Sci. Technol. B **18**, 3168 (2000)

7.6   A.J. DeMarco, J. Melngailis: Lateral growth of focused ion beam deposited platinum for stencil mask repair, J. Vac. Sci. Technol. B **17**, 3154 (1999)

7.7   S. Matsui, T. Kaito, J. Fujita, M. Komuro, K. Kanda, Y. Haruyama: Three-dimensional nanostructure fabrication by focused-ion-beam chemical vapor deposition, J. Vac. Sci. Technol. B **18**, 3181 (2000)

7.8   T. Hoshino, K. Watanabe, R. Kometani, T. Morita, K. Kanda, Y. Haruyama, T. Kaito, J. Fujita, M. Ishida, Y. Ochiai, S. Matsui: Development of three-dimensional pattern-generating system for focused-ion-beam chemical-vapor deposition, J. Vac. Sci. Technol. B **21**, 2732 (2003)

7.9   E. Buks, M.L. Roukes: Stiction, adhesion energy, and the Casimir effect in micromechanical systems, Phys. Rev. B **63**, 033402 (2001)

7.10 J. Fujita, M. Ishida, T. Sakamoto, Y. Ochiai, T. Kaito, S. Matsui: Observation and characteristics of mechanical vibration in three-dimensional nanostructures and pillars grown by focused ion beam chemical vapor deposition, J. Vac. Sci. Technol. B **19**, 2834 (2001)

7.11 M. Ishida, J. Fujita, Y. Ochiai: Density estimation for amorphous carbon nanopillars grown by focused ion beam assisted chemical vapor deposition, J. Vac. Sci. Technol. B **20**, 2784 (2002)

7.12 T. Morita, R. Kometani, K. Watanabe, K. Kanda, Y. Haruyama, T. Hoshino, K. Kondo, T. Kaito, T. Ichihashi, J. Fujita, M. Ishida, Y. Ochiai, T. Tajima, S. Matsui: Free-space-wiring fabrication in nano-space by focused-ion-beam chemical vapor deposition, J. Vac. Sci. Technol. B **21**, 2737 (2003)

7.13 J. Fujita, M. Ishida, Y. Ochiai, T. Ichihashi, T. Kaito, S. Matsui: Graphitization of Fe-doped amorphous carbon pillars grown by focused ion-beam-induced chemical-vapor deposition, J. Vac. Sci. Technol. B **20**, 2686 (2002)

7.14 K. Nakamatsu, K. Yamamoto, T. Hirayama, S. Matsui: Fabrication of fine electron biprism filament by free-space-nanowiring technique of focused-ion-beam + chemical vapor deposition for accurate off-axis electron holography, Appl. Phys. Express **1**, 117004 (2008)

7.15 T. Morita, K. Nakamatsu, K. Kanda, Y. Haruyama, K. Kondo, T. Hoshino, T. Kaito, J. Fujita, T. Ichihashi, M. Ishida, Y. Ochiai, T. Tajima, S. Matsui: Nanomechanical switch fabrication by focused-ion-beam chemical vapor deposition, J. Vac. Sci. Technol. B **22**, 3137 (2004)

7.16 R. Kometani, T. Hoshino, K. Kondo, K. Kanda, Y. Haruyama, T. Kaito, J. Fujita, M. Ishida, Y. Ochiai, S. Matsui: Characteristics of nano-electrostatic actuator fabricated by focused ion beam chemical vapor deposition, Jpn. J. Appl. Phys. **43**, 7187 (2004)

7.17 P. Vukusic, J.R. Sambles: Photonic structures in biology, Nature **424**, 852 (2003)

7.18 K. Watanabe, T. Hoshino, K. Kanda, Y. Haruyama, S. Matsui: Brilliant blue observation from a *Morpho-butterfly*-scale quasi-structure, Jpn. J. Appl. Phys. **44**, L48 (2005)

7.19 R. Kometani, T. Morita, K. Watanabe, K. Kanda, Y. Haruyama, T. Kaito, J. Fujita, M. Ishida, Y. Ochiai, S. Matsui: Nozzle-nanostructure fabrication on glass capillary by focused-ion-beam chemical vapor deposition and etching, Jpn. J. Appl. Phys. **42**, 4107 (2003)

7.20 R. Kometani, T. Hoshino, K. Kondo, K. Kanda, Y. Haruyama, T. Kaito, J. Fujita, M. Ishida, Y. Ochiai, S. Matsui: Performance of nanomanipulator fabricated on glass capillary by focused-ion-beam chemical vapor deposition, J. Vac. Sci. Technol. B **23**, 298 (2005)

7.21 S. Akita, Y. Nakayama, S. Mizooka, Y. Takano, T. Okawa, K.Y. Miyatake, S. Yamanaka, M. Tsuji, T. Nosaka: Nanotweezers consisting of carbon nanotubes operating in an atomic force microscope, Appl. Phys. Lett. **79**, 1691 (2001)

7.22 R. Kometani, T. Hoshino, K. Kanda, Y. Haruyama, T. Kaito, J. Fujita, M. Ishida, Y. Ochiai, S. Matsui: Three-dimensional high-performance nanotools fabricated using focused-ion-beam chemical-vapor-deposition, Nucl. Instrum. Methods Phys. Res. B **232**, 362 (2005)

Part A | 7